



HAL
open science

Synthetic stellar spectra for studying multiple populations in globular clusters. Extended grid, and the effects on the integrated light

Vinicius Branco, Paula R. T. Coelho, Ariane Lançon, Lucimara P. Martins,
Philippe Prugniel

► To cite this version:

Vinicius Branco, Paula R. T. Coelho, Ariane Lançon, Lucimara P. Martins, Philippe Prugniel. Synthetic stellar spectra for studying multiple populations in globular clusters. Extended grid, and the effects on the integrated light. *Astronomy and Astrophysics - A&A*, 2024, 687, 10.1051/0004-6361/202348992 . insu-04650025

HAL Id: insu-04650025

<https://insu.hal.science/insu-04650025v1>

Submitted on 16 Jul 2024

HAL is a multi-disciplinary open access archive for the deposit and dissemination of scientific research documents, whether they are published or not. The documents may come from teaching and research institutions in France or abroad, or from public or private research centers.





L'archive ouverte pluridisciplinaire **HAL**, est destinée au dépôt et à la diffusion de documents scientifiques de niveau recherche, publiés ou non, émanant des établissements d'enseignement et de recherche français ou étrangers, des laboratoires publics ou privés.



Distributed under a Creative Commons Attribution 4.0 International License

Synthetic stellar spectra for studying multiple populations in globular clusters

Extended grid, and the effects on the integrated light

Vinicius Branco^{1,2}, Paula R. T. Coelho¹, Ariane Lançon², Lucimara P. Martins³, and Philippe Prugniel⁴

¹ Universidade de São Paulo, IAG, Rua do Matão, 1226, 05508-090 Sao Paulo, SP, Brazil
e-mail: vbranco@usp.br

² Université de Strasbourg, CNRS, Observatoire astronomique de Strasbourg, UMR 7550, 67000 Strasbourg, France

³ NAT – Universidade Cidade de São Paulo, Rua Galvão Bueno, 868, 01506-000 Sao Paulo, SP, Brazil

⁴ Université de Lyon, LyonI, CRAL-Observatoire de Lyon UMR5574, CNRS, Lyon, France

Received 18 December 2023 / Accepted 16 April 2024

ABSTRACT

Most Galactic globular clusters (GCs) harbour multiple populations of stars (MPs) that are composed of at least two generations: the first generation is characterised by a standard α -enhanced metal mixture, as observed in field halo stars of the Milky Way, and the second generation displays an anti-correlated CN–ONa chemical abundance pattern in combination with an enhanced helium fraction. Adequate collections of stellar spectra are needed to characterize the effect of these changes in the stellar abundance on the integrated light of GCs. We present a grid of synthetic stellar spectra to cover the atmospheric parameters relevant to old stellar populations at four subsolar metallicities and two abundance patterns that are representative of the first and second generations of stars in GCs. The integrated spectra of the populations were computed using our stellar grid and empirical stellar populations, namely, colour-magnitude diagrams from the literature for Galactic GCs. The spectra range from 290 to 1000 nm, where we measured the effect on several spectrophotometric indices due to the surface abundance variations attributed to MPs. We find non-negligible effects of the MPs on the spectroscopic indices that are sensitive to C, N, Ca, or Na, and on the Balmer indices; we also describe how MPs modify specific regions in the near-UV and near-IR that can be measured with narrow or medium photometric passbands. The effects vary with metallicity. A number of these changes remain detectable even when we account for the stochastic fluctuations due to the finite nature of the stellar population cluster.

Key words. atlases – stars: abundances – stars: atmospheres – stars: Population II – globular clusters: general

1. Introduction

It is currently well accepted that most Galactic globular clusters (GCs) are characterised by multiple populations of stars (MPs). Evidence has been found in colour-magnitude diagrams (CMDs) (Piotto et al. 2007; Milone et al. 2013, 2016; Dondoglio et al. 2022; D’Antona et al. 2022), and directly via the spectroscopic determination of star-by-star chemical abundances (Wheeler et al. 1989; Kraft 1994; Kraft et al. 1997; Carretta et al. 2009, 2010). The chemical variations in stars of the same GC are found to be anti-correlated, with one element being depleted while the other is enhanced, such as carbon and nitrogen, oxygen and sodium, and sometimes, magnesium and aluminium (Bragaglia et al. 2010; Gratton et al. 2012; VandenBerg et al. 2022). For an extensive study of MPs in GCs and star clusters in general, we refer to the reviews by Bastian & Lardo (2018), Gratton et al. (2019), and Krumholz et al. (2019).

If Galactic clusters are local representatives of GCs in general, extragalactic GCs (EGCs) should present the same MP phenomenon. The GCs outside of the Milky Way have been extensively studied (e.g. Brodie & Strader 2006; Schiavon et al. 2013; Larsen et al. 2014, 2022; Nardiello et al. 2018; Salaris et al. 2019; D’Abrusco et al. 2022), and the multiple stellar populations have been reported, for example, in the LMC and SMC (e.g. Mucciarelli et al. 2009; Dalessandro et al. 2016;

Niederhofer et al. 2017a,b; Hollyhead et al. 2017; Gilligan et al. 2019; Lagioia et al. 2019; Milone et al. 2020; Saracino et al. 2020; Salgado et al. 2022). While the mechanism behind the formation of MPs is still unknown, the observed integrated spectra of GCs are frequently used to test simple stellar population (SSP) models (see, Lee & Worthey 2005; Percival et al. 2009; Walcher et al. 2009; Vazdekis et al. 2010; Thomas et al. 2011; Martins et al. 2019). It is not yet clear to which extent SSP models that represent systems that are inhomogeneous in terms of chemical abundances may impact the analysis of EGCs (e.g. Larsen et al. 2018).

Efforts have also been directed towards searches for the signatures of MPs in the integrated light of EGCs. For instance, McWilliam & Bernstein (2008) have determined abundances of several elements for 47 Tuc, finding enhanced Na and Al. Studying 31 GCs from M31, Colucci et al. (2009, 2014, 2017) reported correlations of light element abundance ratios with luminosity and velocity dispersion, evidence of variations in the Mg, Na, and Al abundance in GC stars, and a resemblance of Mg, Al (and likely O, Na) measurements of these EGCs to those of Galactic GCs. Colucci et al. (2011) reported that old GCs in the LMC display higher abundance variations of the light elements Mg, Al, and Na than younger GCs, while Schiavon et al. (2013), Sakari et al. (2016, 2021) reported that light-element enhancements show positive correlations with EGC mass. Furthermore, studies have measured

the chemical abundances (Larsen et al. 2022) and metallicities (Sakari & Wallerstein 2022) of the Local Group and outer halo M31 GCs, respectively.

Coelho et al. (2011, 2012, hereafter C11) were the first to predict how the chemical anticorrelations affect the integrated spectrum of stellar populations based on modelling of the integrated light. The authors computed integrated stellar populations with both a standard α -enhanced metal mixture $[\alpha/\text{Fe}] \sim 0.4$ and with an anticorrelated CN–ONa chemical abundances pattern (with and without He enhancement). They provided a quantitative estimate of the maximum effect that a second population would have on the Lick indices for an iron abundance representative of a typical metal-rich Galactic GCs ($[\text{Fe}/\text{H}] = -0.7$). Their results indicate that a second population would increase the equivalent width of some indices (e.g. H_γ , CN_1 , CN_2 , and Na D) and decrease the equivalent width of others (Ca4226, G4300, and Mg_b). These changes go in the direction needed to explain the discrepancies between models and GCs observations when only chemical changes in the α -enhancement are taken into account in SSP models (Chung et al. 2013). The Balmer lines are affected by the second generation of stars when helium enhancement is considered through the change of the turnoff temperature of the underlying isochrone. This effect would imply that an integrated spectrum could appear up to 2–3 Gyr younger than the true age of the population. However, the predictions of C11 were limited to only one iron abundance and to the wavelength range 3500–6000 Å. The effects on a wider range of metallicities and observables remain to be explored.

We aim to expand the study performed by C11 by making a grid of synthetic stellar spectra available for a wider range of metallicities and wavelengths, both for a standard α -enhanced metal mixture and for a composition characteristic of second populations of GCs. The spectra were computed with an optimised combination of existing line lists. They were used to predict the effects of MPs on the integrated spectra of old clusters and spectrophotometric indices as a function of metallicity. Because GCs only contain a finite number of stars, clusters of a given age, composition, and mass can randomly display a range of integrated properties (e.g. Barbaro & Bertelli 1977; Bruzual 2002; Fouesneau & Lançon 2010; Popescu & Hanson 2010; da Silva et al. 2012). We examine to which extent the effects of MPs remain detectable in this stochastic context.

This paper is organised as follows: in Sect. 2 we present the synthetic stellar grid, and in Sect. 3 we describe how the integrated stellar population models were built. We simulate the stochastic populations in Sect. 4 and discuss the results of measured properties in Sect. 5. Our concluding remarks are given in Sect. 6.

2. Synthetic stellar spectra with abundances representative of GC stars

We computed a grid of synthetic stellar spectra suitable for modelling integrated SSPs with old ages, subsolar metallicities, and chemical abundance patterns relevant to GCs. We describe the codes and ingredients we used and the properties of the final grid below.

2.1. Ingredients and codes

The model atmospheres and the synthetic spectra were computed with the Linux ports of the codes ATLAS12 and SYNTHÉ respectively (Kurucz 1970, 2005; Kurucz & Avrett

1981; Kurucz & Furenlid 1979; Sbordone et al. 2004; Sbordone 2005). These codes were adopted in C11 and have been used recently in the study of the integrated data of GCs (Jang et al. 2021; Larsen et al. 2022). For each chemical mixture pattern adopted in this project, we computed the model atmosphere and the synthetic spectrum.

Our atmosphere models were computed using the Opacity Sample method under LTE conditions and 1D plane-parallel geometry. The models were calculated assuming a microturbulence of 1 km s^{-1} , 60 iterations, 72 layers, a mixing length parameter of 1.25, and no overshooting. We adopted the same convergence criteria as Mészáros et al. (2012) for the model atmospheres: the layers were tested to have a difference in flux and flux derivative errors smaller than 1% and 10%, respectively; no more than one non-converged layer was accepted between $\log \tau_{\text{Ross}} = -5$ and $\log \tau_{\text{Ross}} = 1$, where τ_{Ross} is the Rosseland optical depth.

The synthetic spectra were computed with a sampling resolution of 1 700 000, convolved with a Gaussian filter to a spectral resolution of $R = 850\,000$, from 290 nm to 950 nm in air wavelength. Molecular opacities were obtained from R. Kurucz and covered the following molecules¹: AlH [A-X], AlH [B-X], AlO, C_2 [A-X], C_2 [B-A], C_2 [D-A], C_2 [E-A], CaH, CaO, CH, CN [A-X], CN [B-X], CN [X-X], CO [A-X], CO [X-X], CrH [A-X], FeH [F-X], H_2 , MgH, MgO, NaH, NH, OH, SiH, SiO [A-X], SiO [E-X], SiO [X-X], TiH, TiO, and VO. We compiled a new atomic opacity list based on three lists available in the literature, described in Sect. 2.2. The chemical patterns of the grid are discussed in Sect. 2.3.

To automatise the process of computing the grid, we developed a Python wrapper called Python globular cluster synthesizer (hereafter, PyGlobsterS), which combines the ATLAS12 and SYNTHÉ executions and the integration of the SSP spectra (described in Sect. 3). PyGlobsterS decreases the time for computing a large sample of models by allowing it to run in parallel jobs.

2.2. Optimisation of the atomic line list

Different opacities can significantly impact the quality of the synthetic spectrum. Martins & Coelho (2007), for example, tested the accuracy of stellar libraries that assume different opacities and codes, observing that the library with the best average performance employed an atomic line list calibrated against the spectra of the Sun and Arcturus. Recent studies have pointed out the need for accurate opacity lists, not only to describe stars in different evolutionary stages, but also in different regions of the wavelength range (e.g. Martins et al. 2014; Franchini et al. 2018; Lançon et al. 2021).

Based on the purpose of this work, we focused on compiling a list based on literature sources that were available in the format required by SYNTHÉ: Coelho (2014) (hereafter, Coelho14), Kurucz (2018)² (hereafter, Kurucz18), and an updated version of the list by Castelli & Hubrig (2004)³ (hereafter, Castelli16, corresponding to the version of Feb 18th, 2016).

We computed one synthetic solar spectrum for the three atomic lists, keeping the molecular opacities unchanged. In

¹ <http://kurucz.harvard.edu/linelists/linesmol/> (see Table A.1 and Branco 2020 for details.)

² Downloaded from <http://kurucz.harvard.edu/linelists/gfnew/gfall08oct17.dat> on Aug. 8th, 2018.

³ Downloaded from <http://wwwuser.oats.inaf.it/castelli/linelists.html> on Aug. 8th, 2018.

future work, we plan on expanding this study to newer literature on atomic opacities, which were yet to be available when this project started (Larsen et al. 2022; Peterson & Kurucz 2022).

The Sun was chosen as the reference star given its well-defined stellar parameters and the high spectral resolution of the data available in the literature. We considered three determinations for the solar abundances: Grevesse & Sauval (1998), and Asplund et al. (2005, 2009). All solar models adopted $T_{\text{eff}} = 5777$ K, $\log g = 4.4377$ (Cox 2000, 4th. Ed.), and $V_{\text{turb}} = 1.0 \text{ km s}^{-1}$ (Castelli & Kurucz 2003).

The synthetic solar spectra were compared against the solar spectrum obtained from Wallace et al. (2011). This is a high-quality solar spectrum obtained with the Fourier transform spectrometer (FTS) at the McMath-Pierce telescope (as described in Brault 1985), which covers the wavelength region from ~ 2958 – 9250 \AA with a resolution varying from $R = \lambda / \Delta\lambda \sim 350\,000$ – $700\,000$, distributed in six regions (see Table 1 in Wallace et al. 2011). It is a ground-based spectrum corrected for the effect of telluric lines.

We convolved the synthetic spectra to the relevant spectral resolution and used the following metric to quantify the differences between the models and the solar spectrum:

$$\tilde{\Delta}(\lambda) = \frac{1}{N} \sum_{\lambda_1}^{\lambda_2} \left| \frac{f_{\text{synt}}(\lambda_i) - f_{\text{obs}}(\lambda_i)}{f_{\text{obs}}(\lambda_i)} \right|, \quad (1)$$

where N is the number of pixels in the wavelength interval $\Delta\lambda = \lambda_2 - \lambda_1$ centred at λ , and $f_{\text{synt}}(\lambda_i)$ and $f_{\text{obs}}(\lambda_i)$ are the synthetic and observed flux, respectively, at the i th wavelength element.

In Fig. 1 we show the solar spectra computed with the different line lists and $\tilde{\Delta}$ as a function of wavelength to illustrate the behaviour around CaII H&K (top), Mg T (middle), and Na D (bottom). In general, as the wavelength increases, $\tilde{\Delta}$ decreases.

To choose between line lists, we compared the synthetic spectra with the observed solar spectrum over small wavelength intervals of $\Delta\lambda = 0.2 \text{ \AA}$. For each spectral segment, we used Eq. (1) to select the list that best reproduced the solar spectrum (i.e. lowest $\tilde{\Delta}$). The best lists of each segment were combined into a new list covering the whole wavelength interval of the observed spectrum. Table 1 summarises the global performance of each line list (i.e. the $\tilde{\Delta}$ computed over the wavelength range 2958 – 9250 \AA) for three solar abundance patterns. Because the variation among the solar patterns is comparable, we decided to use the most recent reference in the remainder of this article, i.e. Asplund et al. (2009).

2.3. Parameter coverage in the Kiel plane

We aimed at a grid of synthetic spectra suitable to represent GCs of different subsolar metallicities. The grid coverage of the Kiel plane (T_{eff} vs. $\log g$) is based on Milky Way GCs selected from Martins et al. (2019, hereafter, M19), who translated empirical CMDs from Piotto et al. (2002) into the T_{eff} versus $\log g$ plane using the colour transformations from Worthey & Lee (2011). The CMDs were observed with the WFPC2 camera of the Hubble Space Telescope. The PC was centred in the centre of the clusters and covered a field of view of about $2.5' \times 2.5'$.

Based on the CMDs of NGC 1904, NGC 5904, NGC 0104, and NGC 5927, we computed synthetic spectra for the metallicities $[\text{Fe}/\text{H}] = -1.60, -1.29, -0.77,$ and -0.47 , respectively (see Table 2 for metallicity references). The coverage in T_{eff} and $\log g$ is shown in Fig. 2. We considered this coverage appropriate as Sakari et al. (2014) showed that the integrated properties are not

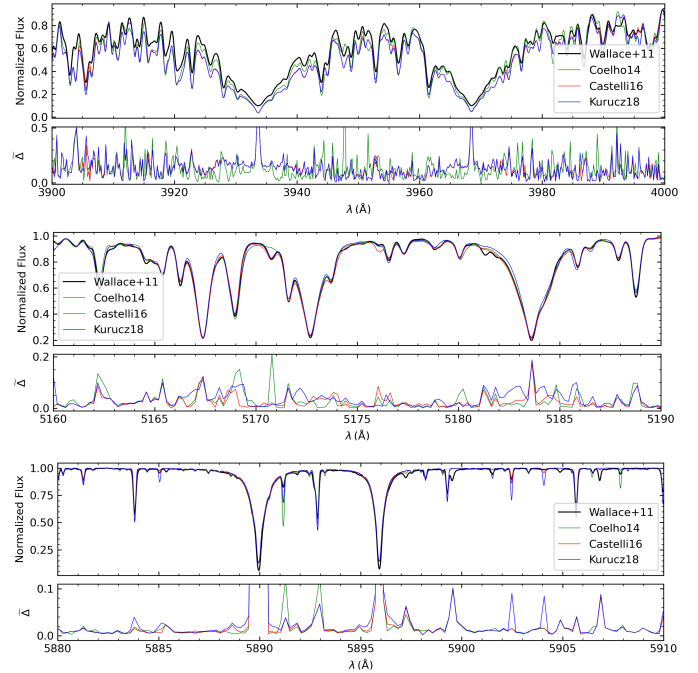


Fig. 1. Comparison between modelled and observed spectra (top panels) and their $\tilde{\Delta}$ (bottom panels) in three regions: CaII H&K (top), Mg T (middle), and Na D (bottom). Each panel shows synthetic spectra computed with the Coelho14 (green), Castelli16 (red), and Kurucz18 (blue) atomic line lists compared to the observed solar spectrum. $\tilde{\Delta}$ is computed according to Eq. (1) with $\lambda_2 - \lambda_1 = 0.2 \text{ \AA}$.

strongly sensitive to the parameter binning in the HR coverage unless the binning is very coarse. The basic data of the selected clusters are shown in Table 2.

For each $[\text{Fe}/\text{H}]$, we considered two chemical abundance patterns:

- A standard metal mixture with $[\alpha/\text{Fe}] \sim 0.4$ and initial He mass fraction $Y = 0.256$ as representative of the first generation (hereafter, 1P), and
- A second generation whose metal composition has C decreased by 0.30 dex, N increased by 1.20 dex, O decreased by 0.45 dex, and Na increased by 0.60 dex with respect to the first-generation α -enhanced mixture, with $Y = 0.300$ (hereafter, 2P). The chemical abundances of the grids are summarised in Table 3.

These choices follow the chemical patterns adopted in C11 for the modelling of a typical metal-rich Galactic GC. They were chosen by these authors based on Carretta et al. (2005) to represent values close to the upper end of the observed anticorrelation in Galactic GCs and to ensure that both populations have the same C+N+O sum to match the assumption of their adopted isochrones.

To keep the assumptions of the grid homogeneous, we adopted the same abundances of CNONa and He in 2P for all the GCs in Table 2. The chosen upper values of CNONa abundances are appropriate for a range in $[\text{Fe}/\text{H}]$ from -2.0 to -0.7 dex (as of Carretta et al. 2005), but may be an extrapolation for our most metal-rich GC.

The synthetic stellar spectra are available in the POLLUX database⁴ and online⁵.

⁴ <https://pollux.oreme.org/>

⁵ <http://specmodels.iag.usp.br>

Table 1. Global performance of each synthetic spectrum computed with different atomic line lists and different solar abundance patterns according to the metric in Eq. (1).

Solar pattern	$\tilde{\Delta}$ Castelli16	$\tilde{\Delta}$ Coelho14	$\tilde{\Delta}$ Kurucz18	$\tilde{\Delta}$ This work
Grevesse & Sauval (1998)	0.9861	0.9894	0.9895	0.9777
Asplund et al. (2005)	0.9842	0.9884	0.9876	0.9763
Asplund et al. (2009)	0.9856	0.9891	0.9891	0.9771

Notes. $\Delta\lambda$ corresponds to 2958–9250 Å, the wavelength range of the observed solar spectrum.

Table 2. GCs selected to guide the atmospheric parameter coverage.

GC	[Fe/H]	Age	$\log M/M_{\odot}$ ^(e)	R_c ^(f)
NGC 5927	-0.49 ^(a)	12.2 ^(b)	5.4	22
NGC 0104	-0.77 ^(d)	12.8 ^(b)	6.0	10
NGC 5904	-1.29 ^(a)	12.2 ^(b)	5.8	26
NGC 1904	-1.60 ^(a)	13.0 ^(c)	5.4	25

Notes. ^(f)Projected core radius in arcmin (Harris 1996, 2010).

References. ^(a)Harris (1996, 2010); ^(b)Dotter et al. (2010); ^(c)De Angeli et al. (2005); ^(d)Carretta et al. (2009); ^(e)Usher et al. (2017).

3. Application to integrated spectra

We computed integrated spectra of stellar populations following the method proposed by M19 (see as well Schiavon et al. 2004; Colucci et al. 2011; Sakari et al. 2014). In short, data from a CMD were converted into the Kiel plane (T_{eff} versus $\log g$) via a colour- T_{eff} transformation. Each star in the Kiel plane was associated with a model in the stellar synthetic grid (the model that was closest to the observed star in atmospheric parameters: see Eq. (3) in M19). The integrated spectrum was obtained by summing the individual model spectra, weighted by the magnitude M_V of the corresponding observed stars.

This approach has the advantage of avoiding uncertainties related to the IMF and isochrone modelling. On the other hand, it has the disadvantage of being sensitive to the sampling of luminous stars and rapid phases, incompleteness of low-mass stars, and mass segregation, if present (see e.g. McWilliam & Bernstein 2008), as the CMD will rarely (if ever) cover the entirety of the GC stars. The CMDs we used in this work were observed with the WFPC2 camera with the PC centred on the cluster centre (Piotto et al. 2002). Considering the core radius of the GCs in Table 2, our models are representative of the central parts of the GCs populations.

The integrated flux F_{λ} of N stars is given by

$$F_{\lambda} = \sum_{i=1}^N f_{\lambda,i} C_i, \quad (2)$$

where f_{λ} is the spectrum of the i th star, and C_i is the weight of the i th star, defined as

$$C_i = \frac{10^{-\frac{M_{V,i}}{2.5}}}{\int T_{\lambda}^V f_{\lambda,i} d\lambda}. \quad (3)$$

Here, $M_{V,i}$ is the absolute magnitude of the i th star, and T_{λ}^V is the response function of the V -band filter.

For each metallicity and chemical pattern, we computed an integrated spectrum, resulting in eight synthetic SSPs. By modelling two simple populations for each iron abundance with

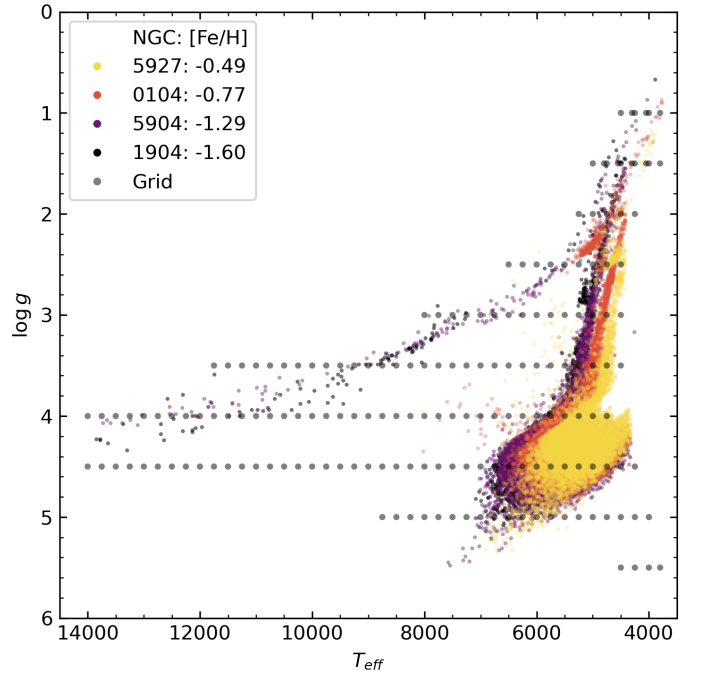


Fig. 2. HRD estimated by Martins et al. (2019) based on observations from Piotto et al. (2002) for NGC5927, NGC0104, NGC5904, and NGC1904, represented by the colored dots. The grey dots indicate the computed spectral models.

extreme chemical pattern values (pure 1P and pure 2P), we estimated an approximate upper level of changes in spectrophotometric features due to CNONa and He variations, rather than to model real GCs. Future work will relax these assumptions to consider varying degrees of chemical changes and 1P/2P proportions (or intermediate subpopulations) as a function of metallicity (Carretta et al. 2009), mass (Schiavon et al. 2013), and radius (Sakari et al. 2014).

The resulting integrated spectra are shown in the left panel in Fig. 3. As expected from the CMDs, the spectral energy distribution of the two most metal-poor cases shows the Balmer features caused by the strong contribution of relatively hot horizontal branch stars. The right panel of the figure shows the ratio of the 2P and 1P reference spectrum for each iron abundance. It shows that the effect of the chemical variations is stronger in the blue region, corresponding to molecules CH, OH, and NH. The feature corresponding to the Na D line is in 5800 Å. Redder than 7000 Å, the signal corresponds to CN molecular band.

The highlighted regions in the right panel in Fig. 3 correspond to wavelength windows with a strong sensitivity to the presence of 2P and are discussed in Sect. 5.

Table 3. Chemical abundance patterns for each SSP.

Grid	[Fe/H]	[α /Fe]	Mixture	Y	H	He	C	N	O	Na
I	-1.58	0.4	1P	0.256	0.92015	0.07980	-3.61	-4.21	-2.95	-5.80
II	-1.58	0.4	2P	0.300	0.90246	0.09749	-3.91	-3.01	-3.40	-5.20
III	-1.29	0.4	1P	0.256	0.92003	0.07987	-3.61	-4.21	-2.95	-5.80
IV	-1.29	0.4	2P	0.300	0.90233	0.09757	-3.91	-3.01	-3.40	-5.20
V	-0.77	0.4	1P	0.256	0.91951	0.08017	-3.61	-4.21	-2.95	-5.80
VI	-0.77	0.4	2P	0.300	0.90174	0.09793	-3.91	-3.01	-3.40	-5.20
VII	-0.47	0.4	1P	0.256	0.91877	0.08059	-3.61	-4.21	-2.95	-5.80
VIII	-0.47	0.4	2P	0.300	0.90090	0.09844	-3.91	-3.01	-3.40	-5.20

Notes. Y is the normalised mass fraction of He, and H to Na are the abundances used in ATLAS12 (H and He are linear number fractions, and C, N, O, and Na are number fractions in logarithmic scale).

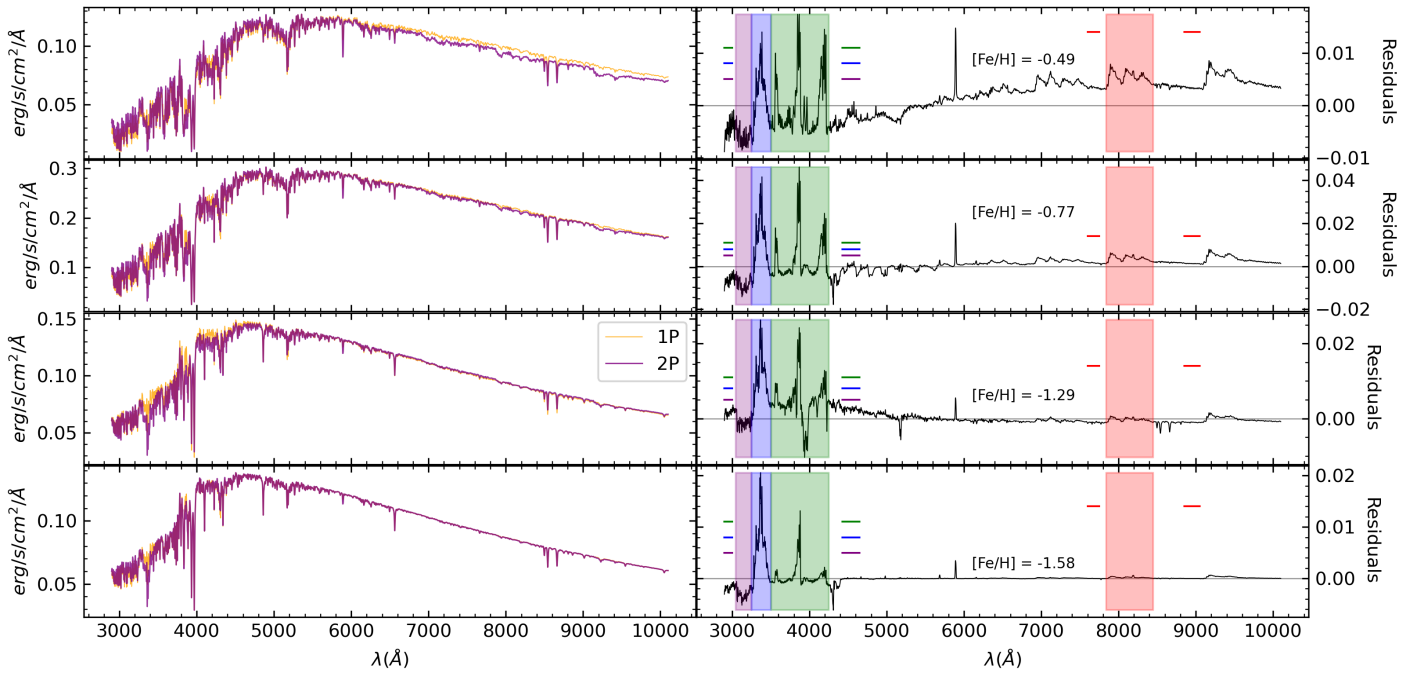


Fig. 3. Comparisons between integrated spectra and regions sensitive to the MPs effects. Left panel: model SSPs. Gen.1 indicates models with the standard mixture of the first generation, i.e. α -enh. Gen.2 represents the modified mixture of the second generation, i.e. α - and Y-enhancements and Δ CNO_{Na} (it also considers the CN–ONa abundance variations). The iron abundances are indicated in the texts in the right panels. Right panel: residual flux between the first- and second-generation spectra for each iron abundance. The wavelength regions affected by the chemical variations typical of the second generation are shown, corresponding to changes in the CH/OH/NH and CN bands and to the Na D line strength. The coloured lines indicate the blue and red continua bandpass intervals that correspond to the central bandpass areas of the same colour.

4. Simulating stochastic populations

GCs may differ by their global physical parameters such as age, metallicity, stellar mass, detailed star formation history, and relative fraction of 1P and 2P stars. Even clusters with the same physical parameters might have different integrated emission spectra due to the stochastic nature of the actual distribution of their finite number of stars, however. The lower the total mass of the cluster, the higher the relative fluctuations in observational properties, such as colours and spectroscopic indices (e.g. Foesneau & Lançon 2010; Cerviño 2013). We examined to which extent the effects of MPs on the integrated light remain detectable in this stochastic context. To this end, we simulated stochastic populations in each of the synthetic SSPs and repeated the comparison between 1P and 2P.

The relative amplitude of stochastic fluctuations depends on the size (total stellar mass) of the stellar population considered,

and this size varies among our four Milky Way GC datasets. Most of the variance comes from bright and short-lived phases, such as the AGB at red or near-infrared wavelengths, or the HB at blue wavelengths, when the HB is extended. In order to bring the four GCs to a common scale, we normalised the CMDs to have the same number of stars in a chosen magnitude range. We chose the upper limit of the luminosity range to be the turn-off point (TO) because the sampling of MS stars is stable against stochastic fluctuations. Regarding the lower luminosity limit, we should consider that the Piotto et al. (2002) observations are magnitude-limited and that therefore, each CMD reaches different depths in the faint MS (closer GCs reach lower masses in the MS). We chose to limit the faintest star to be considered for normalisation to the star closest to $V(\text{TO}) + 1$. Therefore, we split each CMD into two subsamples:

- Subsample A included the stars from the TO down to one magnitude fainter, that is, $V(\text{TO}) \leq V_{\text{star}} \leq V(\text{TO}) + 1$.

Table 4. Data obtained from the isochrones to compute the ratio of subsamples A and B.

Metallicity	Mixture	$V(\text{TO})$	$M_{\text{ini}}(\text{TO})$	$V(\text{TO}) + 1$	$M_{\text{ini}}(V(\text{TO}) + 1)$	$V(\text{TP-AGB})$	$M_{\text{ini}}(\text{TP-AGB})$
-0.49		4.75	0.879	5.75	0.796	-1.08	0.965
-0.77	1P	4.74	0.819	5.73	0.742	-1.43	0.891
-1.29		4.51	0.773	5.51	0.704	-1.86	0.830
-1.60		4.42	0.756	5.41	0.694	-1.93	0.800
-0.49		4.83	0.822	5.82	0.744	-1.13	0.899
-0.77	2P	4.86	0.753	5.85	0.683	-1.47	0.819
-1.29		4.59	0.708	5.59	0.646	-1.86	0.756
-1.60		4.51	0.692	5.49	0.638	-1.88	0.730

Notes. The reference metallicity and chemical mixtures are presented in the first two columns. From the third column on, we show the data obtained from the isochrones: absolute V magnitude in the turn-off [$V(\text{TO})$] and its stellar mass [$M_{\text{ini}}(\text{TO})$]; absolute V magnitude of the nearest-neighbour star one magnitude fainter than the turn-off [$V(\text{TO}) + 1$] and its initial mass [$M_{\text{ini}}(V(\text{TO}) + 1)$]; absolute V magnitude of a star at the beginning of the TP-AGB phase [$V(\text{TP-AGB})$] and its initial mass [$M_{\text{ini}}(\text{TP-AGB})$].

This range is stable against stochastic fluctuations and was used to normalise the number of stars in the four CMDs.

- Subsample B spanned all stars brighter than the TO ($V_{\text{star}} < V(\text{TO})$). This range causes the stochastic fluctuations in the observables (colours and/or indices).

We obtained the position of the TO (that splits subsamples A and B) from the V magnitude predicted from isochrones taken from a Bag of Stellar Tracks and Isochrones (BaSTI; Hidalgo et al. 2018; Pietrinferni et al. 2021)⁶. For each GC, we requested an isochrone with the appropriate cluster age, iron abundance interpolated to that of the target cluster, α -enhancement ($[\alpha/\text{Fe}] = 0.4$), and photometry in the Johnson-Cousins photometric system. The ages and iron abundances adopted are those in Table 2. For the helium mass fraction (Y), we adopted 0.247 and 0.300 for 1P and 2P, respectively.

To relate the number of stars in subsample A to the total number of stars in the cluster, we assumed that the initial stellar mass function (IMF) can be approximated with the universal function of Kroupa (2001). This assumption also allowed us to compute an expected number of stars in the initial mass interval associated with subsample B. The latter is (not surprisingly) not precisely equal to the actual number of stars observed in subsample B. We ran simulations of SSPs drawing stars from the CMDs, with the constraint that every population had the same total number of stars to be integrated. We also enforced that the proportion of stars between subsamples A and B was obtained from the IMF.

Table 4 presents the quantities we used to compute the number of stars. In subsample A, we used the stellar mass of the turn-off $M_{\text{ini}}(\text{TO})$ and the stellar mass of a star that was one magnitude fainter $M_{\text{ini}}(V(\text{TO}) + 1)$. In subsample B, we used the stellar mass in the turn-off $M_{\text{ini}}(\text{TO})$ and the initial mass at the beginning of the TP-AGB phase $M_{\text{ini}}(\text{TP-AGB})$.

For each SSP in Table 4, we built 100 simulated populations, each with 20 000 stars in the mass range between $M_{\text{ini}}(V(\text{TO}) + 1)$ and $M_{\text{ini}}(\text{TPAGB})$, to be representative of GCs with total masses $M \approx 10^5 M_{\odot}$. For subsample A, we bootstrapped the stars only once given that the contribution of these stars is very stable. For subsample B, we bootstrapped the stars 100 times, one for each simulated population. The ratio of the two subsamples was fixed based on the IMF.

Therefore, each mixture and metallicity has 100 bootstrapped populations, normalised to the same total number of stars. Figure 4 illustrates the effect of the stochasticity on the

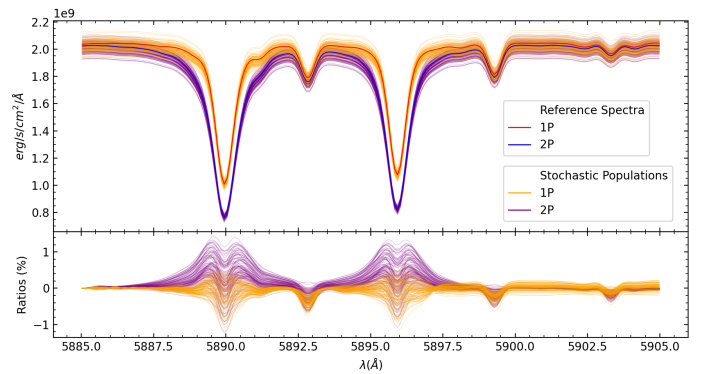


Fig. 4. Stochastic effect in the Na D spectral line. Top: reference integrated spectra for 1P (blue) and 2P (red) and $[\text{Fe}/\text{H}] = -0.77$. The bootstrapped populations of each mixture are shown in orange and purple, respectively. Bottom: Ratios and residuals between bootstrapped and reference integrated spectra.

Na D spectral line for the two chemical mixtures of the metallicity regime relative to NGC 0104, 47Tuc, $[\text{Fe}/\text{H}] = -0.77$. The strength and profile of these strong lines are sensitive to the exact sampling of the stellar mass function. The stochastic effects on the spectrophotometric indices sensitive to the MP are discussed in the next section.

5. Results and discussion

We evaluated the effect of abundance variations between 1P and 2P and related stochastic effects via spectroscopic (Trager et al. 1998) and photometric indices (Milone et al. 2016). All measurements were made with the PYTHON package PYPHOT⁷ (Fouesneau 2022).

5.1. Indices sensitive to multiple populations

The work of C11 identified the Lick indices that are most sensitive to the presence of a 2P, namely CN_1 , CN_2 , Ca4227, G4300, and Na D. We computed these indices in our models for $[\text{Fe}/\text{H}] = -0.77$ (the only metallicity explored in C11) and compare the results in Table 5.

The differences between 1P and 2P from C11 and this work differ in absolute values, but show the same trend. Since the

⁶ <http://basti-iac.oa-abruzzo.inaf.it/isocs.html>

⁷ <https://mfouesneau.github.io/pyphot/index.html>

Table 5. Variations in the Lick indices for $[\text{Fe}/\text{H}] = -0.7$ as in C11 (ΔI_{Coelho}) and those calculated in this work ($\Delta I_{\text{This work}}$), between 1P and 2P.

Index	ΔI_{Coelho}	$\Delta I_{\text{This work}}$
CN ₁	0.084	0.050
CN ₂	0.087	0.052
Ca4227	-0.651	-0.227
G4300	-0.572	-0.813
Na D	1.346	0.785

Table 6. New indices proposed to be sensitive to the MP effects in GCs.

	Bandpasses		
	Blue	Central	Red
OH _{blue}	2900–3000	3050–3250	4430–4650
NH _{blue}	2900–3000	3250–3500	4430–4650
CN _{blue}	2900–3000	3510–4250	4430–4650
CN _{red}	7600–7750	7840–8450	8850–9050

Notes. The bandpasses are defined in angstroms (Å), and the indices are measured in magnitudes.

codes are the same between the two works, we attribute the difference to the opacities. Regarding the molecular opacities, we used the [Masseron et al. \(2014\)](#) opacity table for the CH molecule, which is more recent than the table used in C11. Our atomic line list was refined from literature, as explained in Sect. 2.2.

Inspired by C11 and based on Fig. 3, we propose four new spectral regions that are predicted to be sensitive to the CH, CN, OH, and NH molecular features in the integrated light. The regions were selected by visually inspecting the ratio of 1P and 2P integrated spectra, shown in the right panel of Fig. 3. The features are listed in Table 6 in terms of the usual blue, central, and red bandpasses used in Lick/IDS indices (e.g. [Worthey et al. 1994](#)). The index names OH_{blue}, NH_{blue}, CN_{blue}, and CN_{red} only refer to the dominant species in the central passband (see Fig. 15 in [Coelho et al. 2005](#)), and they are represented in Fig. 3 in pink, purple, green, and red, respectively. The NH index is a narrow-band measurement of the spectral feature that is also measurable with the *Hubble* Space Telescope filters, for instance, with the three-filter index of [Milone et al. \(2013\)](#) that is now commonly used to produce so-called chromosome maps. All measured standard Lick indices as well as other relevant indices from the literature can be found in Table B.1, and we further discuss their behaviour in the next section.

5.2. Effects at different metallicities

Figure 5 shows index-index diagrams with the populations computed in this work. Each panel shows a spectral index from those identified by C11 to be strongly sensitive to MPs versus the metallicity-sensitive index Fe5270. Each dot in the diagrams is a bootstrapped population (Sect. 4).

We confirm the results by C11 that the indices CN₁, CN₂, Ca4227, G4300, and Na D are sensitive to the presence of MPs⁸.

⁸ For conciseness we show CN₁ but not CN₂, which behaves very similarly.

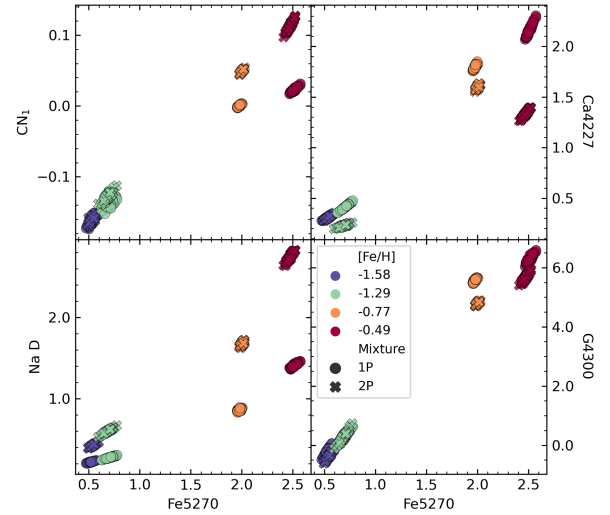


Fig. 5. Stochastic effects in the spectral indices CN₁, Ca4227, G4300, and Na D. Each point in the index-index diagrams corresponds to a population composed of 20 000 stellar models. Each diagram shows 100 populations computed in four metallicity regimes (coloured symbols) and two chemical mixtures (1P and 2P, rounded and x symbols, respectively).

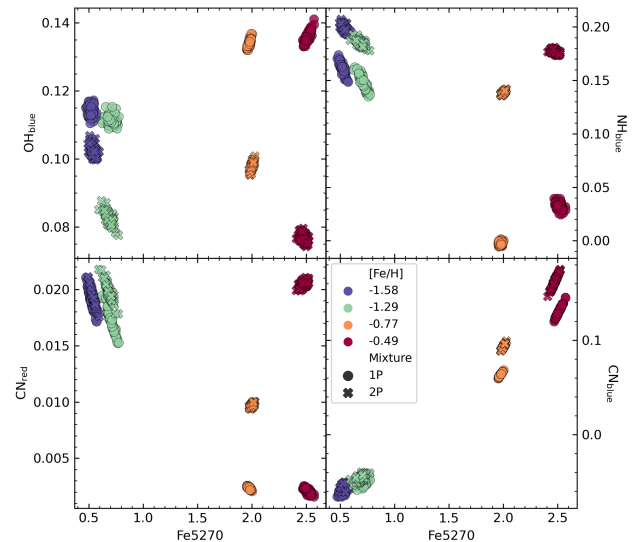


Fig. 6. Same as in Fig. 5; this figure presents the stochastic effects in the new indices proposed to be sensitive to the MP effects in GCs as a function of the metallicity: OH_{blue}, NH_{blue}, CN_{blue}, and CN_{red}.

We also identify that the difference between the 1P and 2P models, represented by the line strengths in the index-index diagrams, generally increases with metallicity. This result was supported by [Sakari et al. \(2016, 2021\)](#) where the increasing Na D line strength indicated an increasing Na-enhanced stellar abundance. The stochastic effect together with typical measurement errors at the two lowest metallicities prevents the separation between 1P and 2P for the indices CN₁, and G4300. At higher metallicities and in the case of Na D, and Ca4227, the separation between 1P and 2P seems to be robust against stochasticity. In any case, we caution that our simulated 1P and 2P are ideal cases illustrating the maximum separations, while in integrated EGCs, we expect to observe a mixture of populations.

Regarding our proposed indices, we show in Fig. 6 that some combinations of indices are robust against the stochastic effects.

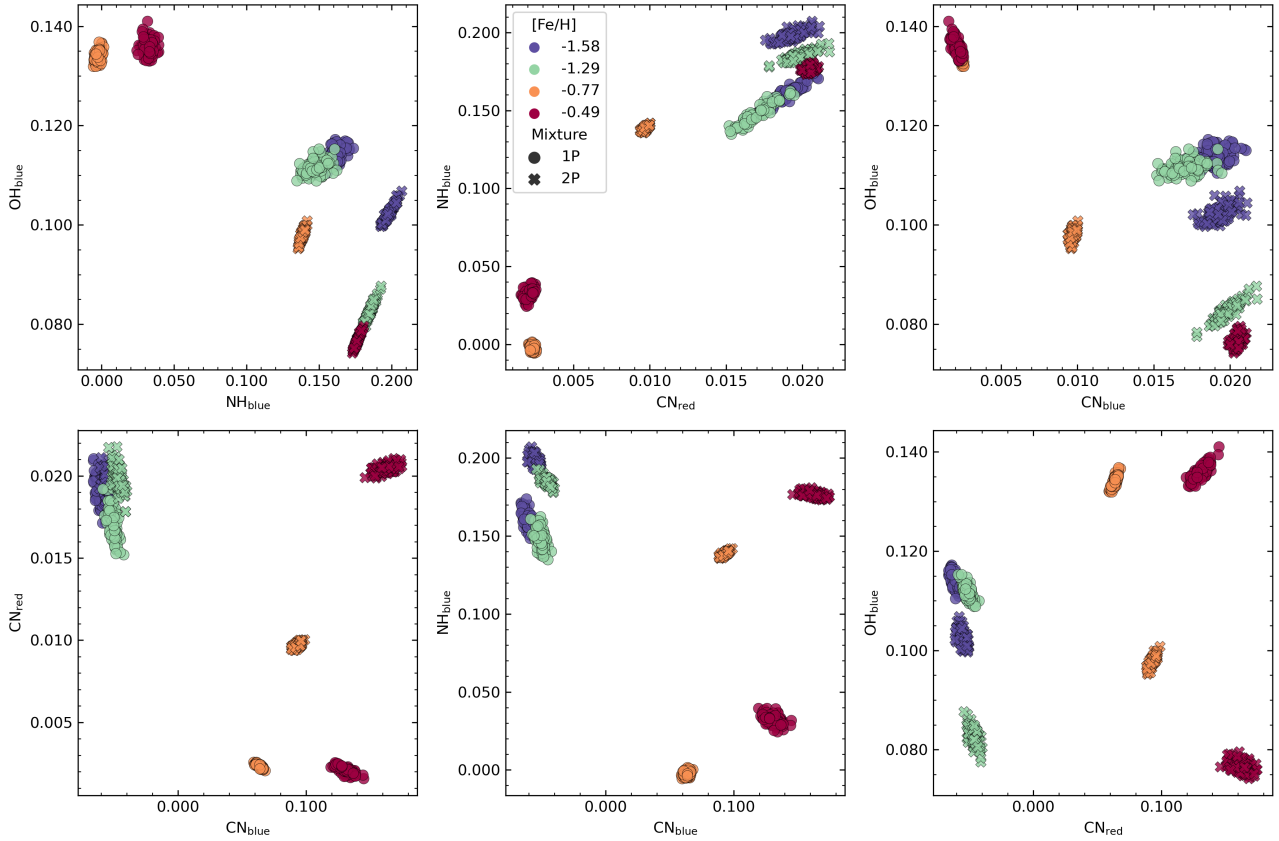


Fig. 7. Same as in Fig. 6; this figure presents index-index diagrams showing the stochastic effects among the new indices proposed to be sensitive to the MP effects in GCs: OH_{blue} , NH_{blue} , CN_{blue} , and CN_{red} .

OH– and NH–Fe5270 diagrams distinguish them well. CN_{red} effectively split the two mixtures in high-metallicity regimes, despite the high dispersion due to stochasticity in low metallicities. CN_{blue} has tighter splits in the high metallicities than its red counterpart, being not as effective as the other indices.

In Fig. 7, we highlight the OH–NH diagram (top left panel), where the groups are well separated. Something similar happens when we compare OH or NH with CN_{red} or CN_{blue} , as in the diagrams of the second row.

We point out the work by Bertone et al. (2020), where a set of new spectral indices was also proposed to identify the MP effects. These authors performed a star-to-star comparison at different evolutionary stages, with four chemical mixture assumptions for a metallicity $[\text{Fe}/\text{H}] = -1.62$; they did not directly examine the indices expected for the integrated light of a cluster. Our methods for producing spectra are slightly different regarding the opacity tables and ATLAS version (ATLAS9 there versus ATLAS12 here). Their synthetic spectra, also computed with SYNTH3, cover a smaller wavelength interval at lower spectral resolutions; our OH_{blue} index (Table 6) lies outside that interval. In Appendix C we present a set of plots with Bertone et al. (2020) spectral indices computed with the integrated spectra of our bootstrapped populations in Fig. C.1, as well as the measurements in Table C.1. We show that their spectral indices, designed to split individual stars of subpopulations, also split 1P and 2P of integrated populations of stars in almost every case.

In Fig. 8, we show a set of diagrams with the bootstrapped populations for each metallicity and chemical mixture that splits 1P and 2P mixtures using HST filters, as suggested in Milone et al. (2013). In the left panel, the colour-colour diagram

uses filters that enhance the separations between populations in the MS and RGB. The middle panel is a chromosome map based on the pseudo-colour index $c(F275W, F336W, F410M)$ ⁹ that intends to maximise the separations. In this panel, instead of filter $F410M$, we used $F438W$ in the combination, along with the $(mF275W - mF438W)$ colour, and this change augmented the separations. After exploring more combinations with the HST filters, we suggest a pseudo-colour diagram with two three-filter indices, $c(F275W, F336W, 438W)$ vs. $c(F275W, F438W, F814W)$, in the right panel. This diagram splits 1P and 2P with a weaker superposition of the bootstrapped populations, thus providing a significant opportunity for measurements of these colours for characterising the MPs using the integrated light of GCs. These photometric indices, among others, are commonly used to identify MPs in colour-magnitude diagrams of Galactic GCs (Gontcharov et al. 2023; Milone et al. 2023a), and they were recently applied to the infrared region with the JWST (Milone et al. 2023b; Ziliotto et al. 2023).

6. Conclusions

The multiple population phenomenon in GCs is an exciting entry point for studying these astrophysical objects. To support these studies, we published a grid of synthetic stellar spectra at four iron abundances and two chemical abundance patterns that characterise GC stars: a standard α -enhanced mixture, and a mixture with anticorrelated CNONa abundances and He enhancement.

Using these spectra, we modelled a total of eight integrated spectra of old stellar populations, a pure 1P and a pure 2P per

⁹ Defined as $(mF275W - mF336W) - (mF336W - mF410M)$.

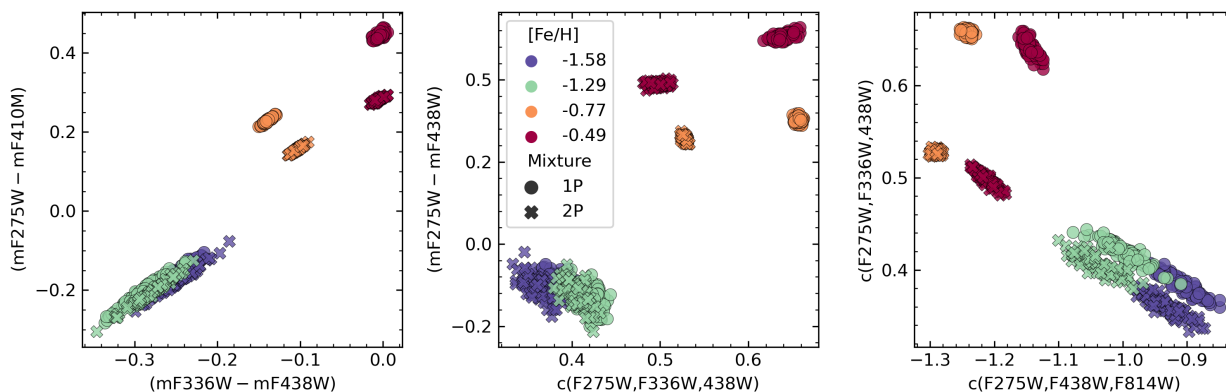


Fig. 8. Same as in Fig. 5; from left to right, this figure presents a colour-colour and two Chromosome-map diagrams.

iron abundance. The synthesis of the integrated light was based on colour-magnitude diagrams of Milky Way GCs and therefore quantifies the effect of GC-specific abundance changes on spectra without accounting for changes in stellar evolution that accompany strong changes in the He abundance. We will address the effects of changes in isochrones in a forthcoming work.

We quantified the effect of different chemical mixtures on spectroscopic indices and narrow/medium photometric passbands by accounting for the stochastic nature of real stellar populations. The effect due to the presence of 2P is detectable in many spectrophotometric indices, and the effect is stronger with increasing iron abundance. In low-metallicities, the stochastic nature of the integrated light of GCs will hamper the detection of a second population.

We suggest four spectral regions that can be used in the studies of MPs in integrated light. Our proposed spectral indices seem to be a promising way of distinguishing populations in index-index diagrams, even in the presence of stochastic effects. For instance, we predict that our proposed $\text{OH}_{\text{blue}}\text{-NH}_{\text{blue}}$ spectral index diagram is a strong indicator of the presence of a second population. We also investigated the behaviour of the chromosome maps when the colours are measured in the integrated light rather than in individual stars. We conclude that the second population may be detected with the following combination of colours: $c(F275W, F336W, 438W)$ versus $c(F275W, F438W, F814W)$.

By measuring spectrophotometric indices in pure 1P and 2P populations, we estimated the interval of possible values when a CNONa-anticorrelated population is present. In real-world GCs, a mixture of these populations or subpopulations will be present, and future work will be dedicated to disentangling these components in the integrated light.

Acknowledgements. This study was financed in part by the Coordenação de Aperfeiçoamento de Pessoal de Nível Superior – Brazil (CAPES) – Finance Code 88887.580690/2020-00 and by Agence Nationale de la Recherche, France, under project POPSICLE (ANR-19-CE31-0022). We also acknowledge the support from Conselho Nacional de Desenvolvimento Científico e Tecnológico (CNPq) under the grants 200928/2022-8, 310555/2021-3, and 307115/2021-6, and from Fundação de Amparo à Pesquisa do Estado de São Paulo (FAPESP) process numbers 2021/08813-7 and 2022/03703-1.

References

Asplund, M., Grevesse, N., & Sauval, A. J. 2005, *ASP Conf. Ser.*, 336, 25
 Asplund, M., Grevesse, N., Sauval, A. J., & Scott, P. 2009, *ARA&A*, 47, 481
 Barbaro, C., & Bertelli, C. 1977, *A&A*, 54, 243
 Bastian, N., & Lardo, C. 2018, *ARA&A*, 56, 83
 Bertone, E., Chávez, M., & Mendoza, J. C. 2020, *MNRAS*, 493, 2195

Bragaglia, A., Carretta, E., Gratton, R., et al. 2010, *A&A*, 519, A60
 Branco, V. 2020, Master's Thesis, IAG – Universidade de São Paulo, Brazil, <https://doi.org/10.11606/D.14.2020.tde-15122020-164651>
 Brault, J. W. 1985, in *High Resolution in Astronomy*, eds. A. O. Benz, M. Huber, & M. Mayor, 3
 Brodie, J. P., & Strader, J. 2006, *ARA&A*, 44, 193
 Bruzual, A. G. 2002, in *Extragalactic Star Clusters*, eds. D. P. Geisler, E. K. Grebel, & D. Minniti, *IAU Symp.*, 207, 616
 Carretta, E., Gratton, R. G., Lucatello, S., Bragaglia, A., & Bonifacio, P. 2005, *A&A*, 433, 597
 Carretta, E., Bragaglia, A., Gratton, R., & Lucatello, S. 2009, *A&A*, 505, 139
 Carretta, E., Bragaglia, A., Gratton, R. G., et al. 2010, *A&A*, 516, A55
 Castelli, F., & Hubrig, S. 2004, *A&A*, 425, 263
 Castelli, F., & Kurucz, R. L. 2003, in *Modelling of Stellar Atmospheres*, eds. N. Piskunov, W. W. Weiss, & D. F. Gray, *Proc. IAU Symp.*, 210, A20
 Cerviño, M. 2013, *New Astron. Rev.*, 57, 123
 Chung, C., Yoon, S.-J., Lee, S.-Y., & Lee, Y.-W. 2013, *ApJS*, 204, 3
 Coelho, P. R. T. 2014, *MNRAS*, 440, 1027
 Coelho, P., Barbuy, B., Meléndez, J., Schiavon, R. P., & Castilho, B. V. 2005, *A&A*, 443, 735
 Coelho, P., Percival, S. M., & Salaris, M. 2011, *ApJ*, 734, 72
 Coelho, P., Percival, S., & Salaris, M. 2012, *Astron. Soc. India Conf. Ser.*, 6, 107
 Colucci, J. E., Bernstein, R. A., Cameron, S., McWilliam, A., & Cohen, J. G. 2009, *ApJ*, 704, 385
 Colucci, J. E., Bernstein, R. A., & McWilliam, A. 2011, *Am. Astron. Soc. Meeting Abstracts*, 217, 328.04
 Colucci, J. E., Bernstein, R. A., & Cohen, J. G. 2014, *ApJ*, 797, 116
 Colucci, J. E., Bernstein, R. A., & McWilliam, A. 2017, *ApJ*, 834, 105
 Cox, A. N. 2000, *Allen's Astrophysical Quantities* (New York: AIP Press)
 D'Abrusco, R., Zegeye, D., Fabbiano, G., et al. 2022, *ApJ*, 927, 15
 Dalessandro, E., Lapenna, E., Mucciarelli, A., et al. 2016, *ApJ*, 829, 77
 D'Antona, F., Milone, A. P., Johnson, C. I., et al. 2022, *ApJ*, 925, 192
 da Silva, R. L., Fumagalli, M., & Krumholz, M. 2012, *ApJ*, 745, 145
 De Angeli, F., Piotto, G., Cassisi, S., et al. 2005, *AJ*, 130, 116
 Dondoglio, E., Milone, A. P., Renzini, A., et al. 2022, *ApJ*, 927, 207
 Dotter, A., Sarajedini, A., Anderson, J., et al. 2010, *ApJ*, 708, 698
 Foesneau, M. 2022, <https://github.com/mfoesneau/pyphot>
 Foesneau, M., & Lançon, A. 2010, *A&A*, 521, A22
 Franchini, M., Morossi, C., Di Marcantonio, P., et al. 2018, *ApJ*, 862, 146
 Gilligan, C. K., Chaboyer, B., Cummings, J. D., et al. 2019, *MNRAS*, 486, 5581
 Gontcharov, G. A., Bonatto, C. J., Rytina, O. S., et al. 2023, *MNRAS*, 526, 5628
 Gratton, R. G., Carretta, E., & Bragaglia, A. 2012, *A&A Rev.*, 20, 50
 Gratton, R., Bragaglia, A., Carretta, E., et al. 2019, *A&A Rev.*, 27, 8
 Grevesse, N., & Sauval, A. J. 1998, *Space. Sci. Rev.*, 85, 161
 Harris, W. E. 1996, *AJ*, 112, 1487
 Harris, W. E. 2010, arXiv e-prints [arXiv:1012.3224]
 Hidalgo, S. L., Pietrinferni, A., Cassisi, S., et al. 2018, *ApJ*, 856, 125
 Hollyhead, K., Kacharov, N., Lardo, C., et al. 2017, *MNRAS*, 465, L39
 Jang, S., Milone, A. P., Lagioia, E. P., et al. 2021, *ApJ*, 920, 129
 Kraft, R. P. 1994, *PASP*, 106, 553
 Kraft, R. P., Snedden, C., Smith, G. H., et al. 1997, *AJ*, 113, 279
 Kroupa, P. 2001, *MNRAS*, 322, 231
 Krumholz, M. R., McKee, C. F., & Bland-Hawthorn, J. 2019, *ARA&A*, 57, 227
 Kurucz, R. L. 1970, *SAO Special Report*, 309
 Kurucz, R. L. 2005, *Mem. Soc. Astron. Ital. Suppl.*, 8, 14
 Kurucz, R. L. 2018, *ASP Conf. Ser.*, 515, 47
 Kurucz, R. L., & Avrett, E. H. 1981, *SAO Special Report*, 391

- Kurucz, R. L., & Furenlid, I. 1979, *SAO Special Report*, 387
- Lagioia, E. P., Milone, A. P., Marino, A. F., & Dotter, A. 2019, *ApJ*, 871, 140
- Lançon, A., Gonneau, A., Verro, K., et al. 2021, *A&A*, 649, A97
- Larsen, S. S., Brodie, J. P., Grundahl, F., & Strader, J. 2014, *ApJ*, 797, 15
- Larsen, S. S., Brodie, J. P., Wasserman, A., & Strader, J. 2018, *A&A*, 613, A56
- Larsen, S. S., Eitner, P., Magg, E., et al. 2022, *A&A*, 660, A88
- Lee, H., & Worthey, G. 2005, *ApJS*, 160, 176
- Martins, L. P., & Coelho, P. 2007, *MNRAS*, 381, 1329
- Martins, L. P., Coelho, P., Caproni, A., & Vitoriano, R. 2014, *MNRAS*, 442, 1294
- Martins, L. P., Lima-Dias, C., Coelho, P. R. T., & Laganá, T. F. 2019, *MNRAS*, 484, 2388
- Masseron, T., Plez, B., Van Eck, S., et al. 2014, *A&A*, 571, A47
- McWilliam, A., & Bernstein, R. A. 2008, *ApJ*, 684, 326
- Mészáros, S., Allende Prieto, C., Edvardsson, B., et al. 2012, *AJ*, 144, 120
- Milone, A. P., Marino, A. F., Piotto, G., et al. 2013, *ApJ*, 767, 120
- Milone, A. P., Piotto, G., Renzini, A., et al. 2016, *MNRAS*, 464, 3636
- Milone, A. P., Marino, A. F., Da Costa, G. S., et al. 2020, *MNRAS*, 491, 515
- Milone, A. P., Cordoni, G., Marino, A. F., et al. 2023a, *A&A*, 672, A161
- Milone, A. P., Marino, A. F., Dotter, A., et al. 2023b, *MNRAS*, 522, 2429
- Mucciarelli, A., Origlia, L., Ferraro, F. R., & Pancino, E. 2009, *ApJ*, 695, L134
- Nardiello, D., Milone, A. P., Piotto, G., et al. 2018, *MNRAS*, 477, 2004
- Niederhofer, F., Bastian, N., Kozhurina-Platais, V., et al. 2017a, *MNRAS*, 465, 4159
- Niederhofer, F., Bastian, N., Kozhurina-Platais, V., et al. 2017b, *MNRAS*, 464, 94
- Percival, S. M., Salaris, M., Cassisi, S., & Pietrinferni, A. 2009, *ApJ*, 690, 427
- Peterson, R. C., & Kurucz, R. L. 2022, *ApJS*, 260, 28
- Pietrinferni, A., Hidalgo, S., Cassisi, S., et al. 2021, *ApJ*, 908, 102
- Piotto, G., King, I. R., Djorgovski, S. G., et al. 2002, *A&A*, 391, 945
- Piotto, G., Bedin, L. R., Anderson, J., et al. 2007, *ApJ*, 661, L53
- Popescu, B., & Hanson, M. M. 2010, *ApJ*, 724, 296
- Sakari, C. M., & Wallerstein, G. 2022, *MNRAS*, 512, 4819
- Sakari, C. M., Venn, K., Shetrone, M., Dotter, A., & Mackey, D. 2014, *MNRAS*, 443, 2285
- Sakari, C. M., Shetrone, M. D., Schiavon, R. P., et al. 2016, *ApJ*, 829, 116
- Sakari, C. M., Shetrone, M. D., McWilliam, A., & Wallerstein, G. 2021, *MNRAS*, 502, 5745
- Salaris, M., Cassisi, S., Mucciarelli, A., & Nardiello, D. 2019, *A&A*, 629, A40
- Salgado, C., Da Costa, G. S., Yong, D., et al. 2022, *MNRAS*, 515, 2511
- Saracino, S., Martocchia, S., Bastian, N., et al. 2020, *MNRAS*, 493, 6060
- Sbordone, L. 2005, *Mem. Soc. Astron. Ital. Suppl.*, 8, 61
- Sbordone, L., Bonifacio, P., Castelli, F., & Kurucz, R. L. 2004, *Mem. Soc. Astron. Ital. Suppl.*, 5, 93
- Schiavon, R. P., Caldwell, N., & Rose, J. A. 2004, *AJ*, 127, 1513
- Schiavon, R. P., Caldwell, N., Conroy, C., et al. 2013, *ApJ*, 776, L7
- Thomas, D., Johansson, J., & Maraston, C. 2011, *MNRAS*, 412, 2199
- Trager, S. C., Worthey, G., Faber, S. M., Burstein, D., & Gonzalez, J. J. 1998, *ApJS*, 116, 1
- Usher, C., Pastorello, N., Bellstedt, S., et al. 2017, *MNRAS*, 468, 3828
- VandenBerg, D. A., Edvardsson, B., Casagrande, L., & Ferguson, J. W. 2022, *MNRAS*, 509, 4189
- Vazdekis, A., Sánchez-Blázquez, P., Falcón-Barroso, J., et al. 2010, *MNRAS*, 404, 1639
- Walcher, C. J., Coelho, P., Gallazzi, A., & Charlot, S. 2009, *MNRAS*, 398, L44
- Wallace, L., Hinkle, K. H., Livingston, W. C., & Davis, S. P. 2011, *ApJS*, 195, 6
- Wheeler, J. C., Sneden, C., & Truran, J. W. Jr 1989, *ARA&A*, 27, 279
- Worthey, G., & Lee, H.-C. 2011, *ApJS*, 193, 1
- Worthey, G., Faber, S. M., Gonzalez, J. J., & Burstein, D. 1994, *ApJS*, 94, 687
- Ziliotto, T., Milone, A., Marino, A. F., et al. 2023, *ApJ*, 953, 62

Appendix A: Molecular line lists

We list the molecular species used in all synthetic spectrum computations. The TiO molecule is not present in the models with $T_{\text{eff}} \geq 4500$ (K) due to computation time and its weak effect in the final spectrum.

Table A.1. List of all molecular opacity species and files used in this work.

Molécula	Diretório	Arquivo
Molecule	Web address	File
AlH [A-X]	http://kurucz.harvard.edu/molecules/alh	alhax.asc
AlH [B-X]	http://kurucz.harvard.edu/molecules/alh	alhxx.asc
AlO	http://kurucz.harvard.edu/molecules/alo	alopatrascu.asc
C ₂ [A-X]	http://kurucz.harvard.edu/linelists/linesmol	c2ax.asc
C ₂ [B-A]	http://kurucz.harvard.edu/linelists/linesmol	c2ba.asc
C ₂ [D-A]	http://kurucz.harvard.edu/molecules/c2	c2dabrookek.asc
C ₂ [E-A]	http://kurucz.harvard.edu/linelists/linesmol	c2ea.asc
CaH	http://kurucz.harvard.edu/molecules/cah	cah.asc
CaO	http://kurucz.harvard.edu/molecules/cao	caoyurchenko.asc
CH	http://kurucz.harvard.edu/molecules/ch	chmasseron.asc
CN [A-X]	http://kurucz.harvard.edu/linelists/linesmol	cnax.asc
CN [B-X]	http://kurucz.harvard.edu/linelists/linesmol	cnbx.asc
CN [X-X]	http://kurucz.harvard.edu/molecules/cn	cnxx12brooke.asc
CO [A-X]	http://kurucz.harvard.edu/linelists/linesmol	coax.asc
CO [X-X]	http://kurucz.harvard.edu/linelists/linesmol	coxx.asc
CrH [A-X]	http://kurucz.harvard.edu/molecules/crh	crhaxbernath.asc
FeH [F-X]	http://kurucz.harvard.edu/molecules/feh	fehfx.asc
H ₂	http://kurucz.harvard.edu/linelists/linesmol	h2.asc
MgH	http://kurucz.harvard.edu/molecules/mgh	mgh.asc
MgO	http://kurucz.harvard.edu/molecules/mgo	mgodaily.asc
NaH	http://kurucz.harvard.edu/molecules/nah	nahrivlin.asc
NH	http://kurucz.harvard.edu/linelists/linesmol	nh.asc
OH	http://kurucz.harvard.edu/molecules/oh	ohupdate.asc
SiH	http://kurucz.harvard.edu/linelists/linesmol	sihnew.asc
SiO [A-X]	http://kurucz.harvard.edu/linelists/linesmol	sioax.asc
SiO [E-X]	http://kurucz.harvard.edu/linelists/linesmol	sioex.asc
SiO [X-X]	http://kurucz.harvard.edu/linelists/linesmol	sioxx.asc
TiH	http://kurucz.harvard.edu/molecules/tih	tih.asc
TiO	http://kurucz.harvard.edu/molecules/tio	tioschwenke.asc
VO	http://kurucz.harvard.edu/molecules/vo	vo.asc

Appendix B: Spectral indices and photometry

All measurements in Table B.1 refer to the chemical mixtures and metallicities of the reference integrated spectra.

Table B.1. Spectral indices and colours of each reference integrated spectrum.

[Fe/H]	-1.58	-1.58	-1.29	-1.29	-0.77	-0.77	-0.49	-0.49
Mixture	1P	2P	1P	2P	1P	2P	1P	2P
CN ₁	0.061	0.191	0.026	0.098	-0.037	-0.009	-0.049	-0.037
CN ₂	0.107	0.239	0.065	0.139	0.005	0.030	-0.010	0.003
Ca4227	2.802	1.776	2.223	1.884	1.099	0.426	0.828	0.758
G4300	6.933	6.528	6.397	5.630	3.770	3.831	3.458	2.886
Na D	1.724	3.311	1.094	2.025	0.492	1.066	0.403	0.758
Fe5270	2.849	2.810	2.254	2.276	1.350	1.352	1.098	1.112
OH _{blue}	0.179	0.106	0.169	0.128	0.126	0.079	0.119	0.092
NH _{blue}	0.081	0.214	0.037	0.175	0.052	0.178	0.046	0.148
CN _{blue}	0.211	0.246	0.117	0.153	0.013	0.040	-0.008	0.005
CN _{blue}	0.000	0.025	0.000	0.012	0.004	0.013	0.004	0.007
[MgFe]	0.471	0.477	0.565	0.406	0.885	0.874	0.881	0.935
(mF336W – mF438W)	-0.251	-0.242	-0.289	-0.276	-0.124	-0.092	0.004	0.003
(mF438W – mF814W)	0.780	0.777	0.829	0.876	1.640	1.626	1.786	1.707
c(F275W,F336W,F438W)	0.376	0.347	0.412	0.397	0.651	0.522	0.636	0.494

Appendix C: Spectral indices proposed in the literature

The Bertone et al. (2020) spectral indices were built upon stellar spectra. Therefore, we show in Figure C.1 how their proposed indices split the subpopulations when applied to the integrated light of a synthetic cluster. Table C.1 shows the measurements of the reference integrated spectra.

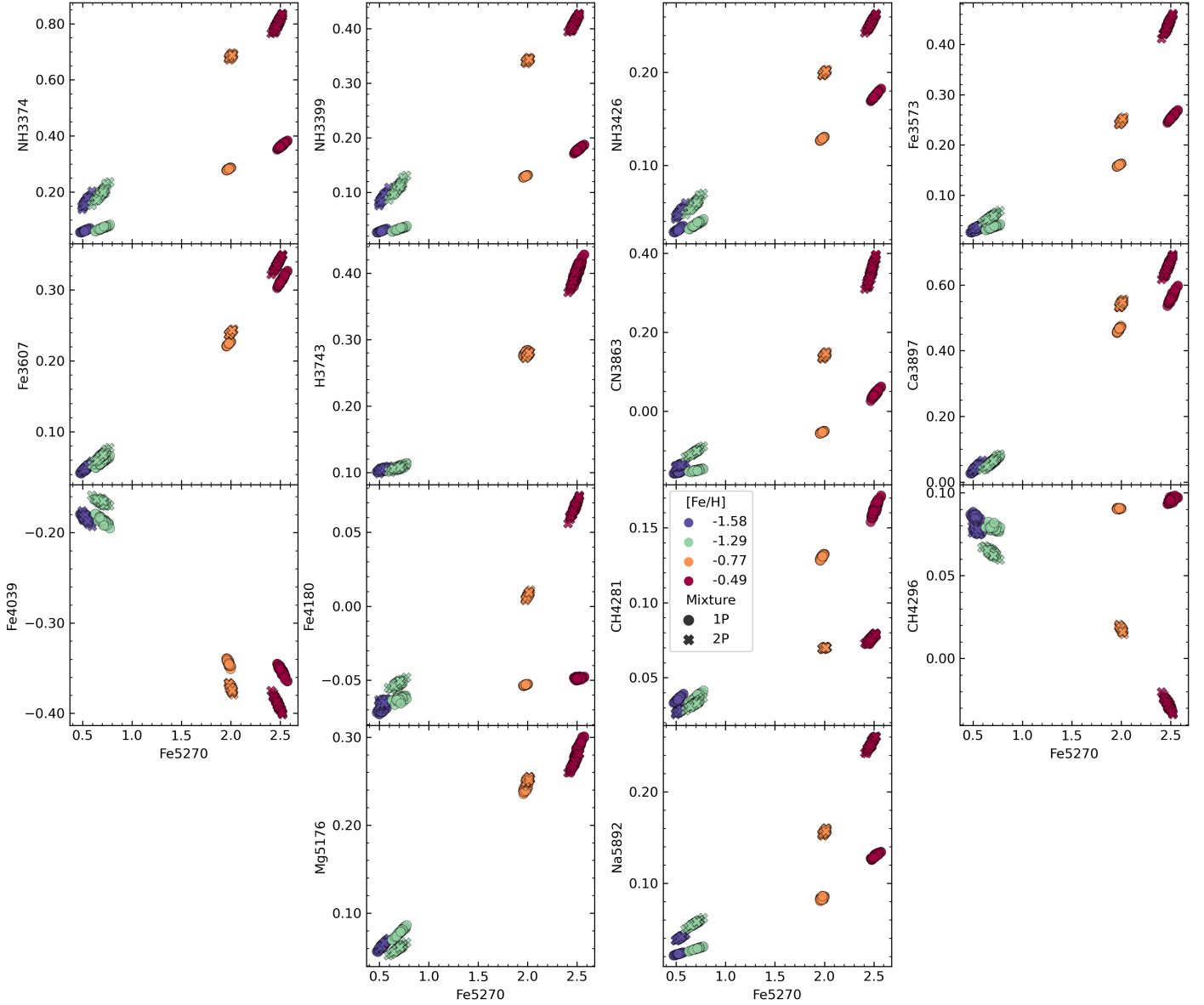


Fig. C.1. Diagrams with proposed spectral indices from the literature computed in the integrated light of different chemical mixture assumptions.

Table C.1. Bertone spectral indices measured with our reference integrated spectra.

[Fe/H]	-1.58	-1.58	-1.29	-1.29	-0.77	-0.77	-0.49	-0.49
Mixture	1P	2P	1P	2P	1P	2P	1P	2P
NH3374	0.445	0.898	0.350	0.765	0.192	0.511	0.172	0.449
NH3399	0.217	0.456	0.161	0.378	0.087	0.272	0.078	0.232
NH3426	0.218	0.304	0.159	0.234	0.087	0.146	0.075	0.125
Fe3573	0.329	0.581	0.203	0.335	0.090	0.167	0.071	0.096
Fe3607	0.381	0.415	0.269	0.289	0.136	0.156	0.110	0.116
H3743	0.513	0.506	0.341	0.330	0.170	0.168	0.140	0.139
CN3863	0.115	0.491	-0.010	0.239	-0.104	0.061	-0.106	-0.028
Ca3897	0.695	0.810	0.567	0.662	0.272	0.282	0.221	0.250
Fe4039	-0.413	-0.472	-0.396	-0.436	-0.273	-0.228	-0.244	-0.250
Fe4180	-0.031	0.126	-0.046	0.043	-0.047	-0.009	-0.048	-0.030
CH4281	0.181	0.077	0.153	0.075	0.089	0.072	0.086	0.058
CH4296	0.087	-0.069	0.093	-0.009	0.074	0.027	0.073	0.046
Mg5176	0.335	0.316	0.269	0.273	0.150	0.109	0.119	0.120
Na5892	0.157	0.305	0.104	0.187	0.049	0.098	0.040	0.071